

# Near-ideal reverse leakage current and practical maximum electric field in $\beta$ -Ga<sub>2</sub>O<sub>3</sub> Schottky barrier diodes

Cite as: Appl. Phys. Lett. **116**, 192101 (2020); doi: 10.1063/5.0007715

Submitted: 16 March 2020 · Accepted: 25 April 2020 ·

Published Online: 11 May 2020



View Online



Export Citation



CrossMark

Wenshen Li,<sup>1,a)</sup>  Devansh Saraswat,<sup>2</sup> Yaoyao Long,<sup>2</sup> Kazuki Nomoto,<sup>1</sup> Debdeep Jena,<sup>1,2,3</sup>  and Huili Grace Xing<sup>1,2,3,a)</sup> 

## AFFILIATIONS

<sup>1</sup>School of Electrical and Computer Engineering, Cornell University, Ithaca, New York 14853, USA

<sup>2</sup>Department of Materials Science and Engineering, Cornell University, Ithaca, New York 14853, USA

<sup>3</sup>Kavli Institute at Cornell for Nanoscale Science, Cornell University, Ithaca, New York 14853, USA

**Note:** This paper is part of the Special Topic on Ultrawide Bandgap Semiconductors.

<sup>a)</sup>Authors to whom correspondence should be addressed: [w1552@cornell.edu](mailto:w1552@cornell.edu) and [grace.xing@cornell.edu](mailto:grace.xing@cornell.edu)

## ABSTRACT

We investigate the intrinsic reverse leakage mechanisms in Ni-based Schottky barrier diodes (SBDs) fabricated on a  $(\bar{2}01)$  single crystal  $\beta$ -Ga<sub>2</sub>O<sub>3</sub> substrate, where a uniform bulk reverse leakage current has been designed and confirmed. The temperature-dependent reverse leakage characteristics are analyzed by a numerical reverse leakage model, which includes both the image-force lowering and doping effects. We found that the reverse leakage current is near-ideal and dominated by Schottky barrier tunneling throughout the entire range of the surface electric field from 0.8 MV/cm to 3.4 MV/cm. The extracted barrier height from the reverse leakage model is consistent with the values extracted from the forward current–voltage and capacitance–voltage measurements. The practical maximum electric field, defined by the maximum allowable reverse leakage current levels, is calculated as a function of the barrier height. These results suggest that it is possible to approach the intrinsic breakdown electric field in  $\beta$ -Ga<sub>2</sub>O<sub>3</sub> SBDs, as long as a sufficiently high barrier height ( $\sim 2.2$  to 3 eV) is employed.

Published under license by AIP Publishing. <https://doi.org/10.1063/5.0007715>

$\beta$ -Ga<sub>2</sub>O<sub>3</sub> has been under intensive research as a promising ultrawide-bandgap semiconductor material.<sup>1</sup> It is expected to have a high breakdown electric field of up to 8 MV/cm due to the sizable bandgap of 4.5–4.7 eV,<sup>2–3</sup> as well as a decent electron mobility of up to  $\sim 200$  cm<sup>2</sup>/V s.<sup>4,5</sup> These properties yield a Baliga figure-of-merit (BFOM) higher than GaN and 4H-SiC, thus making Ga<sub>2</sub>O<sub>3</sub> a strong material candidate for high power devices.<sup>6</sup> In addition, melt-growth techniques for Ga<sub>2</sub>O<sub>3</sub> substrates are available,<sup>7</sup> which promises a cost-effective device platform.

The past few years have witnessed fast-paced advancements in Ga<sub>2</sub>O<sub>3</sub> power devices. Over 2-kV Schottky barrier diodes (SBDs),<sup>8–10</sup> as well as high-voltage power transistors<sup>11–14</sup> have been demonstrated. A high BFOM of 0.95 GW/cm<sup>2</sup> has been achieved in trench SBDs,<sup>15</sup> which is already comparable with that in state-of-the-art GaN unipolar devices.

Due to the difficulty in native p-type doping,<sup>16</sup> Schottky barrier diodes may be the most important rectifiers in Ga<sub>2</sub>O<sub>3</sub>. Although promising performance in Ga<sub>2</sub>O<sub>3</sub> SBDs has been demonstrated, there have not been many studies on the intrinsic reverse leakage mechanisms in Ga<sub>2</sub>O<sub>3</sub> SBDs. This subject is of high importance since the

breakdown voltage or maximum surface electric field ( $E_{\text{max}}$ ) of SBDs based on wide-bandgap semiconductors is typically limited by the leakage current, rather than the material's breakdown electric field. Understanding the intrinsic leakage current mechanisms will allow accurate evaluation of  $E_{\text{max}}$  practically allowable in SBDs, which we refer to as the *practical maximum electric field*.

Previous studies on the leakage mechanisms have been carried out mostly under relatively low surface electric fields ( $E$ ) below 2 MV/cm, where thermionic emission (TE)<sup>17,18</sup> or thermionic-field emission (TFE)<sup>19–21</sup> dominates. To observe and identify the intrinsic reverse leakage current, especially under a higher surface electric field, several challenges need to be addressed. First, edge leakage current due to electric-field crowding should be suppressed and uniform bulk leakage current should be confirmed. We have shown that the edge leakage in small devices and/or with very low doping concentrations in the drift layer can be prominent even with  $E < 1$  MV/cm.<sup>20</sup> Second, the material and Schottky interface need to be of high-enough quality such that the defect-related leakage process is insignificant. Third, the image-force lowering (IFL) effect should be properly considered in

the analysis of the leakage characteristics, which is especially critical for the TE and TFE currents. Previous reports have claimed Poole–Frenkel,<sup>22</sup> trap-assisted-tunneling,<sup>23,24</sup> and variable-range hopping processes<sup>21–24</sup> in Ga<sub>2</sub>O<sub>3</sub> SBDs, which we believe most likely resulted from one or combinations of these three challenges in studying SBDs, but not necessarily the material quality of Ga<sub>2</sub>O<sub>3</sub> alone.

In this work, by addressing the three challenges outlined above, we are able to observe and identify near-ideal reverse leakage current of Ga<sub>2</sub>O<sub>3</sub> SBDs up to a surface electric field of 3.4 MV/cm. In addition, the practical maximum electric field in  $\beta$ -Ga<sub>2</sub>O<sub>3</sub> SBDs is calculated as a function of the barrier height.

Under a high surface electric field in SBDs, tunneling processes—TFE and FE (field emission)—dominate the reverse leakage current. TFE and FE processes have been analytically examined by Murphy and Good,<sup>25</sup> and later by Padovani and Stratton.<sup>26</sup> However, Murphy and Good's models assume a triangular barrier, and thus, the doping effect in semiconductors is not considered.<sup>25</sup> Padovani and Stratton's models consider the doping effect; however, IFL is neglected.<sup>26</sup> To properly include both the IFL and doping effects, we developed a numerical reverse leakage model for the analysis of the reverse leakage characteristics.

The total reverse leakage current density ( $J$ ) is given by<sup>25</sup>

$$J = \frac{A^* T}{k_B} \int_{\mathcal{E}_{\min}}^{+\infty} \mathcal{T}(\mathcal{E}) \times \ln \left[ 1 + \exp \left( -\frac{\mathcal{E} - \mathcal{E}_{\text{Fm}}}{k_B T} \right) \right] d\mathcal{E}, \quad (1)$$

where  $A^* = 4\pi m^* k_B^2 e/h^3$  is the Richardson constant,  $\mathcal{E}$  is the electron energy,  $\mathcal{E}_{\text{Fm}}$  is the Fermi-level energy in metal, and  $\mathcal{E}_{\min}$  is the minimum energy for the tunneling process to occur, which is equal to the effective constant potential energy inside the metal.<sup>25</sup>  $\mathcal{T}(\mathcal{E})$  is the transmission probability across the barrier. If  $\mathcal{E}_{\text{Fm}}$  is taken as the zero-energy level, the potential energy distribution of the Schottky barrier under IFL is given by

$$\mathcal{E}_c(x) = e\phi_B - eEx - \frac{e^2}{16\pi\epsilon_s x} + \frac{e^2 N_D x^2}{2\epsilon_s}, \quad (2)$$

where  $\phi_B$  is the Schottky barrier height,  $E$  is the surface electric field,  $N_D$  is the net donor concentration, and  $\epsilon_s$  is the dielectric constant of  $\beta$ -Ga<sub>2</sub>O<sub>3</sub> ( $10 \epsilon_0$ ).<sup>27</sup> The 3rd and 4th terms in Eq. (2) capture the IFL effect and the doping effect, respectively. Due to IFL, the top of the barrier is rounded and lowered by  $\Delta\phi = \sqrt{eE/(4\pi\epsilon_s)}$ , such that  $\mathcal{E}_{c,\max} = e(\phi_B - \Delta\phi)$ , as illustrated in Fig. 1(a). It is important to consider this barrier-rounding effect in detail for an accurate evaluation of the tunneling probability, by using Eq. (2). It may be tempting to simply replace  $\phi_B$  with  $\phi_B - \Delta\phi$  to reflect IFL, as shown in Fig. 1(b). However, this would significantly overestimate the tunneling probability and, thus, an improper way of treating IFL. Under a Wentzel–Kramers–Brillouin (WKB)-type approximation,  $\mathcal{T}(\mathcal{E})$  is given by<sup>25</sup>

$$\mathcal{T}(\mathcal{E}) = \begin{cases} \left[ 1 + \exp \left( -\frac{2i}{\hbar} \int_{x_1}^{x_2} p(x) dx \right) \right]^{-1}, & \text{if } \mathcal{E} \leq \mathcal{E}_{c,\max} \\ 1, & \text{if } \mathcal{E} > \mathcal{E}_{c,\max}, \end{cases} \quad (3)$$

where  $p(x) = -i\sqrt{2m^*(\mathcal{E}_c(x) - \mathcal{E})}$  and  $x_1$  and  $x_2$  are classical turning points, where  $\mathcal{E}_c(x) = \mathcal{E}$ . Here,  $\mathcal{E}_{c,\max}$  naturally separates the two reverse leakage current components: tunneling (when  $\mathcal{E} \leq \mathcal{E}_{c,\max}$ ) and thermionic emission with IFL (when  $\mathcal{E} > \mathcal{E}_{c,\max}$ ). The integrand in Eq. (1) starts to decrease exponentially as the electron energy  $\mathcal{E}$  decreases beyond a few  $k_B T$  below  $\mathcal{E}_{\text{Fm}}$ , and thus,  $\mathcal{E}_{\min}$  can be safely replaced by  $-\infty$ . Since the effective mass of conduction band electrons

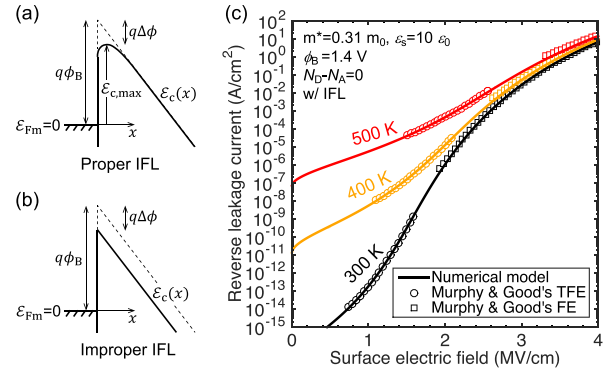


**FIG. 1.** Schematic illustration of the barrier potential distribution under reverse bias (a) with image-force lowering (IFL) properly considered and (b) with IFL improperly considered. (c) Calculated reverse leakage current as a function of the surface electric field in  $\beta$ -Ga<sub>2</sub>O<sub>3</sub> Schottky barrier diodes (SBDs) using our numerical model, with image-force lowering properly considered but without the doping effect. The model agrees well with Murphy and Good's thermionic field emission (TFE) and field emission (FE) models<sup>25</sup> within their applicable ranges.

in  $\beta$ -Ga<sub>2</sub>O<sub>3</sub> is almost isotropic and there is no valley degeneracy,<sup>28</sup> we use a single effective mass for both the Richardson constant and the tunneling effective mass, with a value of  $0.31 m_0$ .<sup>29</sup>

Figure 1(c) shows the calculated reverse leakage current using our numerical model with  $\phi_B = 1.4$  V. To compare with Murphy and Good's analytical models, the doping concentration is temporarily taken as zero to mimic the same condition. It can be seen that our model matches very well with Murphy and Good's TFE and FE models within their respective applicable ranges. This validates our numerical methods. *In the subsequent data analysis, the doping effect will be explicitly considered in our numerical model.*

Ni-Ga<sub>2</sub>O<sub>3</sub> SBDs were fabricated on (201) Sn-doped  $\beta$ -Ga<sub>2</sub>O<sub>3</sub> bulk substrates, as schematically shown in Fig. 2(a). The wafer was cleaned with acetone and methanol first and then soaked in HF and HCl for 5 min each to remove surface defects that might have resulted from wafer polishing or storage. The fabrication process begins with a deposition of Ti/Au (75/150 nm) for the cathode Ohmic contact on the backside of the wafer, followed by a rapid thermal annealing at 470 °C for 1 min under N<sub>2</sub> ambience to facilitate the Ohmic contact. Subsequently, the anode area is defined by photolithography followed by surface treatments consisting of a 5-min ozone treatment and acid cleaning using 30:1 buffered oxide etchant (BOE) and 1:1 diluted HCl each for 1 min to remove photoresist residues. Ni/Pt (50/30 nm) anode Schottky contacts were deposited by electron-beam evaporation and patterned by lift-off. Ga<sub>2</sub>O<sub>3</sub> is prone to plasma-induced surface damage,<sup>30</sup> and thus, the Schottky contact surface was not exposed to any plasma process throughout the fabrication process. Finally, a self-aligned dry etching (0.5  $\mu$ m) was performed for mesa isolation using a BCl<sub>3</sub>/Ar gas mixture,<sup>31</sup> with the anode metal as the hard mask. The etched sidewall is nearly vertical.<sup>32</sup> This serves as an effective edge termination based on similar principles as shown in vertical GaN p–n diodes.<sup>33</sup>

Temperature-dependent capacitance–voltage ( $C$ - $V$ ) and forward and reverse current–voltage ( $I$ - $V$ ) measurements were performed on the fabricated SBDs. Figure 2(b) shows the extracted net doping concentration ( $N_D - N_A$ ) from  $C$ - $V$  measurements, which show a nearly constant value of  $\sim 1.45 \times 10^{18} \text{ cm}^{-3}$ . The inset shows the  $1/C^2$ - $V$

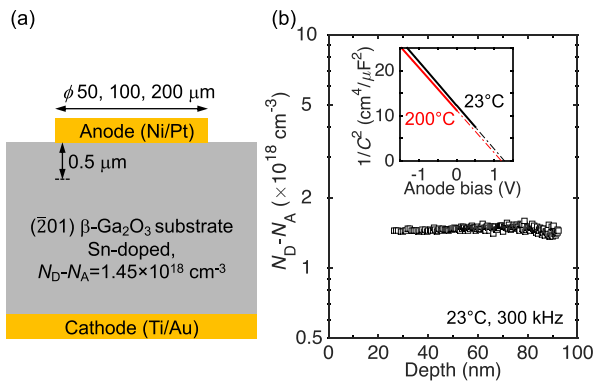


**FIG. 2.** (a) Schematic of Ni-Ga<sub>2</sub>O<sub>3</sub> SBDs fabricated on a Sn-doped (201) β-Ga<sub>2</sub>O<sub>3</sub> bulk substrate. A self-aligned mesa isolation with an etch depth of 0.5 μm is employed for edge termination. (b) Extracted net doping concentration from C–V measurements, showing a near constant value of 1.45 × 10<sup>18</sup> cm<sup>-3</sup>. The inset shows the 1/C<sup>2</sup>–V plot, which is used to extract the barrier height from the extrapolated built-in potential.

plot, which is used to extract the barrier height from the extrapolated built-in potential at zero bias ( $V_{bi,0}$ ) (see, for example, the method described in Ref. 19).  $V_{bi,0}$  values are found to be 1.30 V at 23 °C and 1.23 V at 200 °C.

Figure 3(a) shows the temperature-dependent forward  $I$ – $V$  characteristics. The thermionic emission (TE) model is used to extract the apparent barrier height ( $\phi_{B,ap}$ ) as well as the ideality factor ( $n$ ) by fitting the experimental data to

$$J_{TE} = A^* T^2 \exp\left(-\frac{e\phi_{B,ap}}{k_B T}\right) \left[\exp\left(\frac{eV_F}{nk_B T}\right) - 1\right] = J_0 \left[\exp\left(\frac{eV_F}{nk_B T}\right) - 1\right], \quad (4)$$

where  $V_F$  is the forward bias,  $A^*$  has a value of 37 A cm<sup>-2</sup> K<sup>-2</sup> using  $m^* = 0.31 m_0$ , and  $J_0$  is the saturation current density; a  $J_0$  value of 1 mA/cm<sup>2</sup> corresponds to a  $\phi_{B,ap}$  value of ~0.6 V at room temperature (RT). The extracted barrier heights and ideality factors are shown in Fig. 3(b). The ideality factor is 1.14 at 23 °C and decreases to 1.05 at 200 °C. Since the surface electric field at zero bias ( $E_0 = \sqrt{2(N_D - N_A)(eV_{bi,0} - k_B T)/\epsilon_s}$ ) is as high as 0.8 MV/cm due to the high doping concentration, IFL cannot be neglected. Using the

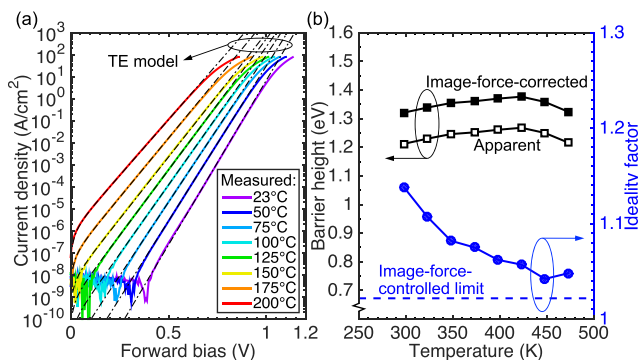


**FIG. 3.** (a) Temperature dependence of the forward  $I$ – $V$  characteristics. Thermionic emission (TE) model is used for the data analysis. (b) Extracted barrier height and ideality factor from the TE model.

standard method,<sup>34</sup> the image-force correction ( $\Delta\phi_{if}$ ) to the apparent height is calculated to be 0.11 V, and the image-force controlled limit for the ideality factor ( $n_{if}$ ) is 1.022. After image-force (IF) correction, the barrier height is around 1.35 eV, as shown in Fig. 3(b). The slight temperature dependence of the extracted barrier height could be due to a finite but nearly negligible presence of barrier inhomogeneity<sup>23,35</sup> or interface trapping.<sup>20</sup>

The reverse  $I$ – $V$  characteristics were first tested at room temperature on diodes with different diameters. Figure 4 shows the typical measured  $I$ – $V$  curves. We have confirmed that the reverse current density has no dependence on the anode diameter, as shown in the inset of Fig. 4. This serves as a solid evidence that the edge leakage is sufficiently suppressed and that the bulk leakage current dominates. The reverse  $I$ – $V$  characteristics can be very well-fitted using our numerical model, with the barrier height being the only fitting parameter. The barrier height value of 1.37 eV is very close to the IF-corrected barrier height extracted from forward  $I$ – $V$  measurements. Also shown in Fig. 4 is the calculation using Murphy and Good’s field emission model with IFL considered.<sup>25</sup> Due to the absence of the doping effect in Murphy and Good’s FE model, the current density is overestimated by roughly a factor of 2; but the voltage/electric-field dependence is captured fairly well, indicating that the FE process is the dominant reverse leakage process at RT in our SBDs. Clearly, the numerical reverse leakage model offers better accuracy in this high-doping case, but the difference is not significant. Hence, Murphy and Good’s analytical model, where the doping effect is neglected, is still a very good one to calculate the ideal leakage current in power devices since the doping level is typically lower than what is used in this work.

Figure 5 shows the temperature-dependent reverse leakage current density as a function of the surface electric field ( $J$ – $E$  characteristics). Throughout the range of surface electric fields (0.8 MV/cm–3.4 MV/cm) and at each temperature, the reverse  $J$ – $E$  characteristics can be well-fitted by our numerical model, again with the barrier height as the only fitting parameter. This suggests that the measured reverse leakage current is near-ideal. Furthermore, we have plotted the thermionic emission components alone within the total reverse leakage currents. It can be seen that the contribution of thermionic

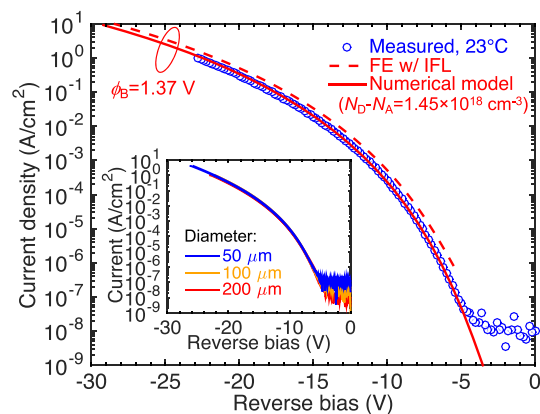


**FIG. 4.** Representative measured reverse  $I$ – $V$  characteristics at RT and the calculations using our numerical model and Murphy and Good’s FE model. Inset: reverse  $I$ – $V$  characteristics on devices with different diameters (three devices per group) at RT, showing no size dependence.

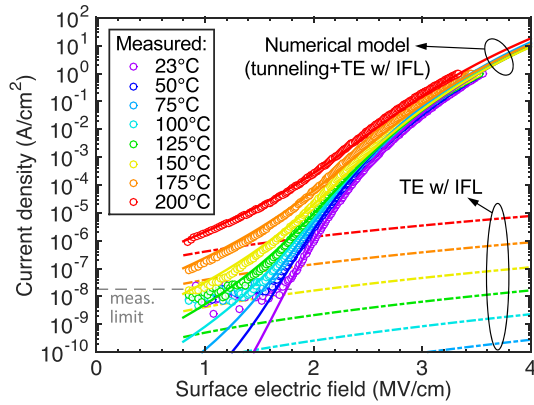


**FIG. 5.** Temperature-dependent reverse leakage current density as a function of the surface electric field ( $J$ - $E$  characteristics). The numerical reverse leakage model is used for data fitting, with the barrier height being the only fitting parameter. The contribution from thermionic emission (TE) alone in the presence of image-force lowering (IFL) is also shown.

emission throughout the electric field range is insignificant, and thus, the main leakage mechanism in these SBDs is barrier tunneling.

To further verify the barrier tunneling process: TFE or FE, the Fowler–Nordheim (F–N) plot, or  $J/E^2$ - $1/E$  plot was generated from the temperature-dependent reverse  $J$ - $E$  characteristics, as shown in Fig. 6. The curve at RT shows good linearity in the F–N plot, characteristic of the FE process. On the other hand, the curves start to deviate from linearity as temperature increases, especially when the surface electric field is low, suggesting the presence of TFE. The transition from FE to TFE with the decrease in the surface electric field is as expected, as shown previously in Fig. 1(c).

The barrier height values extracted from the reverse  $I$ - $V$  characteristics are in excellent agreement with the values extracted from the forward  $I$ - $V$  characteristics [Fig. 7(a)] and  $C$ - $V$  measurements [Fig. 7(b)], with a maximum difference of only 0.06 eV. This further supports the validity of our numerical reverse leakage modeling that considers of both IFL and doping effects properly.

Using the numerical reverse leakage model, we calculate the maximum practical surface electric field as a function of the barrier height in  $\beta$ -Ga<sub>2</sub>O<sub>3</sub> SBDs, defined at a maximum reverse leakage current density ( $J_{\max}$ ) of 1 mA/cm<sup>2</sup> or 100 mA/cm<sup>2</sup>, as shown in Fig. 8. The value of 1 mA/cm<sup>2</sup> is the typical reverse leakage current density at the rated blocking voltage in commercial SBDs,<sup>36</sup> and 100 mA/cm<sup>2</sup> serves as a more relaxed criterion. To allow for generalization of the results, the doping effect is neglected in the calculation. This can be justified since the absence of the doping effect will not induce significant errors. Specifically, we have verified that even with a net doping concentration of  $2 \times 10^{18}$  cm<sup>-3</sup>, the maximum error induced by neglecting the doping effect is smaller than 0.09 MV/cm. Excellent agreement is observed between our calculation and experimental data, both from this work and from the literature.<sup>23,24,37</sup> The near-ideal reverse leakage characteristics in those previously reported SBDs were not recognized, likely because a comprehensive analysis was not performed.

It can be seen that the practical  $E_{\max}$  increases almost linearly with the barrier height. This suggests that it is possible to reach an  $E_{\max}$  value close to the intrinsic breakdown electric field of  $\beta$ -Ga<sub>2</sub>O<sub>3</sub> (6–8 MV/cm) as long as a sufficiently high barrier height (>2.2 eV) is implemented. In

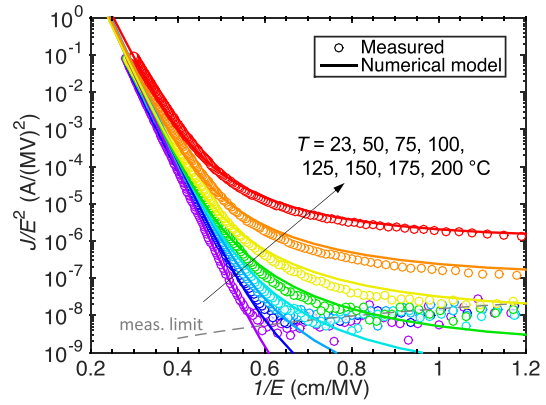


**FIG. 6.** Fowler–Nordheim (F–N) plot of the temperature-dependent reverse  $J$ - $E$  characteristics, as well as the fitting using the numerical reverse leakage model.

fact, Schottky barrier heights of 2.2–2.4 eV have been realized with oxidized metal contacts on  $\beta$ -Ga<sub>2</sub>O<sub>3</sub>,<sup>35</sup> and thus, this possibility may become a reality in the future. A further increase in the barrier height beyond half of the bandgap energy may be very challenging.<sup>35</sup> However, interfacial dipole engineering could be exploited as a potential way to increase the barrier height even further, as demonstrated in Ref. 38.

It is worth noting that below a threshold barrier height value, the calculated practical  $E_{\max}$  drops to zero. This means that below this threshold barrier height, the diode saturation current  $J_0$  exceeds the pre-defined maximum leakage currents  $J_{\max}$ . According to the ideal diode  $I$ - $V$  equation without barrier tunneling, which is essentially Eq. (4) assuming  $n = 1$ , an ideal diode will allow a current flow at  $J_0$  when a reverse bias is higher than a few times the thermal voltage  $k_B T/e$ . SBDs with a  $\phi_B$  value lower than the threshold value can still be made of course, but they suffer from leakage currents higher than the  $J_{\max}$  desired by power electronics.

In conclusion, with the edge leakage suppressed and plasma damage to the Schottky contact interface avoided, near-ideal reverse leakage current is observed in  $\beta$ -Ga<sub>2</sub>O<sub>3</sub> SBDs up to a surface electric field of 3.4 MV/cm. The reverse leakage characteristics can be well-fitted with our numerical model, which considers both the image-force lowering and the doping effects properly. Throughout the whole electric field

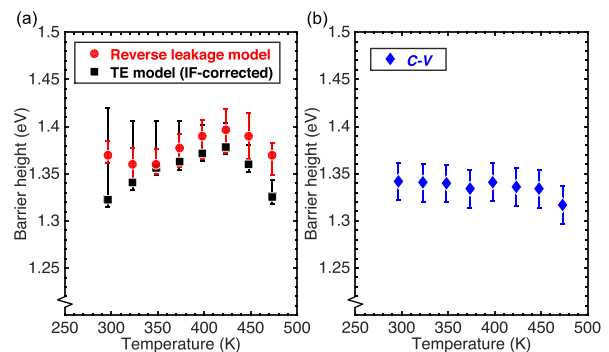


**FIG. 7.** Extracted barrier heights from (a) forward and reverse  $I$ - $V$  characteristics; (b)  $C$ - $V$  measurements. Good agreement between different extracted methods is observed with a maximum difference of  $\sim 0.06$  eV.

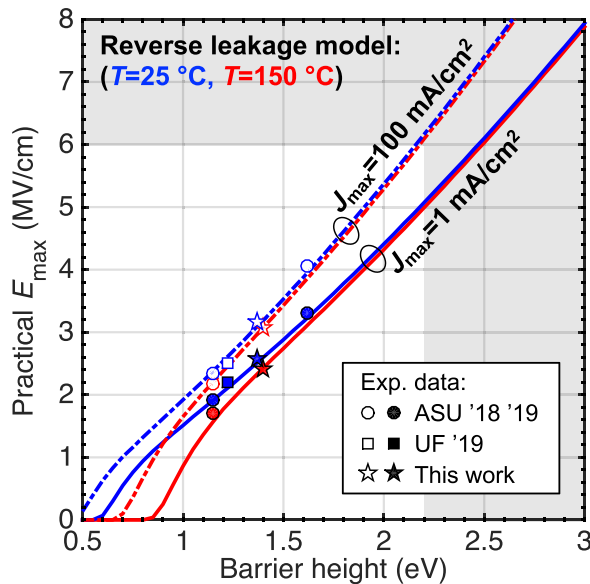


**FIG. 8.** Calculated practical maximum electric field ( $E_{\max}$ ) in  $\beta$ -Ga<sub>2</sub>O<sub>3</sub> SBDs defined at fixed maximum reverse leakage current density levels ( $J_{\max} = 1 \text{ mA/cm}^2$ ,  $100 \text{ mA/cm}^2$ ), as a function of the barrier height. The doping effect is neglected in the calculations, but the results are applicable to a wide range of doping concentrations, with a maximum error of 0.09 MV/cm when  $N_D - N_A \leq 2 \times 10^{18} \text{ cm}^{-3}$  and 0.21 MV/cm when  $N_D - N_A \leq 5 \times 10^{18} \text{ cm}^{-3}$ . Experimental data from this work and from the literature<sup>23,24,37</sup> are also shown (hollow for  $J_{\max} = 100 \text{ mA/cm}^2$  and solid for  $J_{\max} = 1 \text{ mA/cm}^2$ ).

range of 0.8 MV/cm–3.4 MV/cm, near-ideal barrier tunneling dominates the leakage current instead of thermionic emission or trap-assisted tunneling. The practical maximum electric field, defined by the maximum allowable reverse leakage current levels, is calculated as a function of the barrier height. The results suggest the possibility of approaching the intrinsic breakdown electric field in Ga<sub>2</sub>O<sub>3</sub> SBDs with a sufficiently high barrier height of  $\sim 2.2$  to 3 eV but no need to utilize the entire bandgap of the semiconductor. This implies that there is no need to develop p–n homojunctions in Ga<sub>2</sub>O<sub>3</sub>, and a high-quality p–n heterojunction with a sufficiently large built-in potential will serve well in designing Ga<sub>2</sub>O<sub>3</sub> power electronic devices. This study also confirms the excellent material quality of  $\beta$ -Ga<sub>2</sub>O<sub>3</sub> since no signature of trap-assisted tunneling is observed, while providing valuable guidance toward the design of high-voltage and low-leakage Schottky barrier diodes.

This work was supported in part by NSF DMREF 1534303 and AFOSR (Nos. FA9550-17-1-0048 and FA9550-18-1-0529) and carried out at the Cornell Nanoscale Facility and CCMR Shared Facilities sponsored by the NSF NNCI program (No. ECCS-1542081), the MRSEC program (No. DMR-1719875), and MRI DMR-1338010.

#### DATA AVAILABILITY

The data that support the findings of this study are available within this article.

#### REFERENCES

- <sup>1</sup>M. Higashiwaki and G. H. Jessen, *Appl. Phys. Lett.* **112**, 060401 (2018).
- <sup>2</sup>M. Higashiwaki, K. Sasaki, A. Kuramata, T. Masui, and S. Yamakoshi, *Appl. Phys. Lett.* **100**, 013504 (2012).

- <sup>3</sup>K. Ghosh and U. Singiseti, *J. Appl. Phys.* **124**, 085707 (2018).
- <sup>4</sup>Z. Feng, A. F. M. Anhar Uddin Bhuiyan, M. R. Karim, and H. Zhao, *Appl. Phys. Lett.* **114**, 250601 (2019).
- <sup>5</sup>N. Ma, N. Tanen, A. Verma, Z. Guo, T. Luo, H. Xing, and D. Jena, *Appl. Phys. Lett.* **109**, 212101 (2016).
- <sup>6</sup>M. Higashiwaki, K. Sasaki, H. Murakami, Y. Kumagai, A. Koukitu, A. Kuramata, T. Masui, and S. Yamakoshi, *Semicond. Sci. Technol.* **31**, 034001 (2016).
- <sup>7</sup>A. Kuramata, K. Koshi, S. Watanabe, Y. Yamaoka, T. Masui, and S. Yamakoshi, *Jpn. J. Appl. Phys., Part 1* **55**, 1202A2 (2016).
- <sup>8</sup>W. Li, Z. Hu, K. Nomoto, R. Jinno, Z. Zhang, T. Q. Tu, K. Sasaki, A. Kuramata, D. Jena, and H. G. Xing, in 2018 IEEE International Electron Devices Meeting (IEDM) (2018), p. 8.5.1.
- <sup>9</sup>Z. Hu, H. Zhou, Q. Feng, J. Zhang, C. Zhang, K. Dang, Y. Cai, Z. Feng, Y. Gao, X. Kang, and Y. Hao, *IEEE Electron Device Lett.* **39**, 1564 (2018).
- <sup>10</sup>J. Yang, F. Ren, M. Tadjer, S. J. Pearton, and A. Kuramata, *ECS J. Solid State Sci. Technol.* **7**, Q92 (2018).
- <sup>11</sup>Z. Hu, K. Nomoto, W. Li, N. Tanen, K. Sasaki, A. Kuramata, T. Nakamura, D. Jena, and H. G. Xing, *IEEE Electron Device Lett.* **39**, 869 (2018).
- <sup>12</sup>W. Li, K. Nomoto, Z. Hu, T. Nakamura, D. Jena, and H. G. Xing, in 2019 IEEE International Electron Devices Meeting (IEDM) (2019), p. 12.4.1.
- <sup>13</sup>K. Zeng, A. Vaidya, and U. Singiseti, *Appl. Phys. Express* **12**, 081003 (2019).
- <sup>14</sup>K. Tetzner, E. B. Treidel, O. Hilt, A. Popp, S. B. Anooz, G. Wagner, A. Thies, K. Ickert, H. Gargouri, and J. Würfl, *IEEE Electron Device Lett.* **40**, 1503 (2019).
- <sup>15</sup>W. Li, K. Nomoto, Z. Hu, D. Jena, and H. G. Xing, *IEEE Electron Device Lett.* **41**, 107 (2020).
- <sup>16</sup>A. Kyrtos, M. Matsubara, and E. Bellotti, *Appl. Phys. Lett.* **112**, 032108 (2018).
- <sup>17</sup>K. Konishi, K. Goto, H. Murakami, Y. Kumagai, A. Kuramata, S. Yamakoshi, and M. Higashiwaki, *Appl. Phys. Lett.* **110**, 103506 (2017).
- <sup>18</sup>C. Hou, R. M. Gazoni, R. J. Reeves, and M. W. Allen, *IEEE Electron Device Lett.* **40**, 1587 (2019).
- <sup>19</sup>M. Higashiwaki, K. Konishi, K. Sasaki, K. Goto, K. Nomura, Q. T. Thieu, R. Togashi, H. Murakami, Y. Kumagai, B. Monemar, A. Koukitu, A. Kuramata, and S. Yamakoshi, *Appl. Phys. Lett.* **108**, 133503 (2016).
- <sup>20</sup>W. Li, K. Nomoto, Z. Hu, D. Jena, and H. G. Xing, in 2019 Device Research Conference (DRC) (2019), p. 209.
- <sup>21</sup>B. Wang, M. Xiao, X. Yan, H. Y. Wong, J. Ma, K. Sasaki, H. Wang, and Y. Zhang, *Appl. Phys. Lett.* **115**, 263503 (2019).
- <sup>22</sup>L. Zhou, X. Lu, L. Chen, X. Ouyang, B. Liu, J. Xu, and H. Tang, *ECS J. Solid State Sci. Technol.* **8**, Q3054 (2019).
- <sup>23</sup>H. Fu, H. Chen, X. Huang, I. Baranowski, J. Montes, T. H. Yang, and Y. Zhao, *IEEE Trans. Electron Devices* **65**, 3507 (2018).
- <sup>24</sup>T. H. Yang, H. Fu, H. Chen, X. Huang, J. Montes, I. Baranowski, K. Fu, and Y. Zhao, *J. Semicond.* **40**, 012801 (2019).
- <sup>25</sup>E. L. Murphy and R. H. Good, Jr., *Phys. Rev.* **102**, 1464 (1956).
- <sup>26</sup>F. A. Padovani and R. Stratton, *Solid State Electron.* **9**, 695 (1966).
- <sup>27</sup>B. Hoeneisen, C. A. Mead, and M.-A. Nicolet, *Solid State Electron.* **14**, 1057 (1971).
- <sup>28</sup>H. Peelaers and C. G. Van de Walle, *Phys. Status Solidi B* **252**, 828 (2015).
- <sup>29</sup>Y. Zhang, A. Neal, Z. Xia, C. Joishi, J. M. Johnson, Y. Zheng, S. Bajaj, M. Brenner, D. Dorsey, K. Chabak, G. Jessen, J. Hwang, S. Mou, J. P. Heremans, and S. Rajan, *Appl. Phys. Lett.* **112**, 173502 (2018).
- <sup>30</sup>J. Yang, S. Ahn, F. Ren, R. Khanna, K. Bevilin, D. Geerapuram, S. J. Pearton, and A. Kuramata, *Appl. Phys. Lett.* **110**, 142101 (2017).
- <sup>31</sup>L. Zhang, A. Verma, H. G. Xing, and D. Jena, *Jpn. J. Appl. Phys., Part 1* **56**, 030304 (2017).
- <sup>32</sup>W. Li, Z. Hu, K. Nomoto, Z. Zhang, J. Y. Hsu, Q. T. Thieu, K. Sasaki, A. Kuramata, D. Jena, and H. G. Xing, *Appl. Phys. Lett.* **113**, 202101 (2018).
- <sup>33</sup>H. Fukushima, S. Usami, M. Ogura, Y. Ando, A. Tanaka, M. Deki, M. Kushimoto, S. Nitta, Y. Honda, and H. Amano, *Jpn. J. Appl. Phys., Part 1* **58**, SCCD25 (2019).
- <sup>34</sup>W. Mönch, *J. Vac. Sci. Technol., B* **17**, 1867 (1999).
- <sup>35</sup>C. Hou, R. M. Gazoni, R. J. Reeves, and M. W. Allen, *IEEE Electron Device Lett.* **40**, 337 (2019).
- <sup>36</sup>See <http://www.wolfspeed.com/power/products/sic-schottky-diodes/table> for “SiC Schottky Diodes” (last accessed February 13, 2020).
- <sup>37</sup>P. H. Carey, J. Yang, F. Ren, R. Sharma, M. Law, and S. J. Pearton, *ECS J. Solid State Sci. Technol.* **8**, Q3221 (2019).
- <sup>38</sup>T. Harada, S. Ito, and A. Tsukazaki, *Sci. Adv.* **5**, eaax5733 (2019).